Dielectric behavior of the frog lens in the 100 Hz to 500 MHz range

Simulation with an allocated ellipsoidal-shells model

Makio Watanabe, Toshinobu Suzaki, and Akihiko Irimajiri
Department of Physiology, Kochi Medical School, Nankoku, Kochi 783, Japan

ABSTRACT In an attempt to correlate the passive electrical properties of the lens tissue with its structure, we measured ac admittances for isolated frog lenses, lens nuclei, and homogenate of cortical fiber cells, over the frequency range $10^2 - 5 \cdot 10^8$ Hz. The whole lenses molded into discoid shape show a characteristic "two-step" dielectric dispersion with a huge permittivity increment of the order of 10^5 at 1 kHz. Of the two subdispersions disclosed, *dispersion* 1 has a permittivity increment ($\Delta\epsilon$) of $2 \cdot 10^5$ with a characteristic frequency (f_c) of 2 kHz, and *dispersion* 2 has a $\Delta\epsilon$ of 400 with an f_c of 2 MHz. In terms of loss tangent, these dispersions are more clearly located as two separate peaks. Data are analyzed using an allocated ellipsoidal-shells model which has been developed by taking into account fiber orientation inside the lens tissue. *Dispersion* 1 is assigned to the equatorial cortex, where fiber cells run parallel to the applied electric field, and *dispersion* 2 to the nucleus with a complex fiber arrangement and also to the polar cortex, in which the fiber alignment is predominantly perpendicular. In addition, the model analysis reveals that, in the frog lens, the nucleus occupies ~30% in volume and that relative permittivity and conductivity for the cell interior are, respectively, 45 and 3 mS/cm for the cortical cells, and 28 and 0.3 mS/cm for the nuclear cells.

INTRODUCTION

The lens of the eye is a unique tissue. Transparency is a prerequisite for a normal lens to function despite its densely proteinaceous nature; the state of impaired vision due to lens turbidity is called the cataract. Structurally, the major part of the lens consists of a mass of rather featureless fibrous cells that lack intracellular membranes such as the nucleus and mitochondria. In addition, the lens is an avascular tissue and hence can be easily isolated as an intact entity. Although such simplicity appears to allow the lens to be characterized in full detail, much is not known. For instance, the cellular mechanism(s) responsible for lens transparency still remains to be elucidated in spite of many research efforts so far made. To establish a comprehensive view of this unique tissue, inclusive of a clue to cataractogenesis, exploitation of different approaches is desirable. In particular, nondestructive techniques other than the optical ones that enable probing the lens as a whole, once developed, would find a wide scope of application.

The electrial properties of a living tissue can be a good measure of the functional state of the membrane and cytoplasm of the cells involved in it. Pauly and Schwan (1964) carried out dielectric measurements on three identifiable parts of the bovine lens at frequencies from 0.5 to 200 MHz and described a β-type dispersion that is attributable to the limiting membrane of lens fiber cells. Duncan (1969*a–c*) proposed the hypothesis that the lens as a whole can be regarded electrically as a giant cell. Since then, many electrophysiological studies using the micropipette technique have been made to delineate the mode of ion movement inside the lenticular tissue, on the basis of equivalent-circuit analyses at subkilohertz frequencies (Eisenberg and Rae, 1976; Mathias et al., 1979, 1981; Rae et al., 1982). In a much higher frequency range of 10 MHz–10 GHz, Grant and colleagues measured, by time domain spectroscopy, passive electrical properties of several ocular tissues including the lens cortex and nucleus (Dawkins et al., 1981; Gabriel et al., 1983). To the authors' knowledge, however, studies exploring the dielectric properties of intact lenses over a wide enough frequency range to disclose the β and other types of dispersions are lacking. Also missing have been attempts to interpret lens impedance data in terms of a realistic cell model other than the conventional equivalent-circuit model.

In this paper, we first describe the lens dielectric behavior as examined over six decades of frequencies up to 500 MHz, followed by its analysis based on a simplified, but realistic, model which takes into account both the cell shape and fiber orientation peculiar to this tissue. The results show that frog lenses give rise to at least two dominant dispersions in differing frequency ranges and that these are successfully assigned, through model simulations, to pertinent regions in the lens architecture, thereby enabling us to estimate the permit-

Dr. T. Suzaki's present address is Faculty of Integrated Arts and Sciences, Hiroshima University, Hiroshima 730, Japan.
Address correspondence to Dr. A. Irimajiri.

0006-3495/91/01/139/11 $2.00

tivity and conductivity of fiber cells from outside of the tissue.

MATERIALS AND METHODS

Preparation of lens samples

Adult bullfrogs *Rana catesbeiana,* weighing 300–400 g, purchased from a local supplier, were used in this study. After the animal was doubly pithed, the globes were removed and the lenses were carefully extracted by a posterior approach. Lenses that were not clear or with capsular injury were discarded. Before dielectric measurements, the lenses were rinsed in amphibian saline (composition in millimolars: 103 NaCl, 1.0 KCl, 0.9 $CaCl_2$, and 1.2 $NaHCO_3$; pH 7.3) and gently blotted with filter paper to remove excess fluid from the surface. Nuclei were isolated by stripping the lens specimens, using a blunt scalpel, until a characteristic resistance was felt at the cortical/nuclear border. These isolated frog lenses and nuclei, both being nearly spherical, measured respectively ~6 and ~4 mm in average diameter in the equatorial plane.

Homogenate of cortical tissue was prepared by using a miniature glass homogenizer. Cortical scrapings pooled from 6–8 lenses were triturated into paste, with no additives except when testing for the effect of surfactant. In this latter case, 20 mg of digitonin was added to ~0.5 ml of homogenate, followed by mixing with several further strokes of the pestle. In case air bubbles were entrapped in the resulting homogenate, these were purged by centrifugation at 10,000 × *g* for 5 min.

Measuring cells and mounting of sample

The main part of the dielectric cell (Fig. 1), designed for measurements on lenses and nuclei, consisted of a Pt-disc electrode pair of adjustable separation and a fitted sliding sleeve. The electrode diameter was 9 mm for whole lenses and 6 mm for nuclei. The cell constant, stray capacitance, and residual inductance varied with electrode separation, so that we determined these "constants" for each electrode pair at several separations (1–4 mm), using standard KCl solutions. The cell constants thus obtained agreed within 3% with those calculated from cell geometry. Data reduction for a specific measurement was performed using a pertinent set of "constants" that were obtained by interpolation.

The procedure for mounting the whole lenses was as follows. After the cell was disassembled, the specimen was placed on the fixed (*bottom*) electrode with its anterior pole facing the center of the electrode, covered with the sleeve over its equatorial surface, and subsequently compressed between the movable (*top*) electrode and the fixed one until practically no free space remained inside the cavity. Electrode separation was then measured by a micrometer. Nuclei were mounted in a similar manner except that a greater compression stress was applied. It should be here noted that this maneuver of mild "molding" was quite effective for defining the dimensions of a specimen and also for reducing artifacts due to electrode polarization, which, unless properly controlled, often blurred the details of tissue dielectric dispersion at such low frequencies as applied in the present study.

For measurements on homogenate, which was highly viscous, we occasionally employed a coaxial cell with a wide-bored sample inlet to facilitate loading of samples.

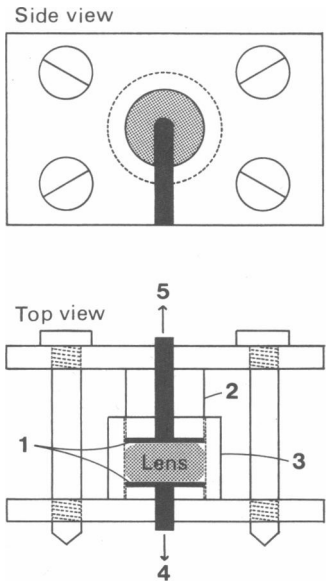

FIGURE 1 Schematic of the cell employed. (1) Pt-disc electrodes (platinized), (2) Lucite cylinder with electrode, (3) Lucite sleeve (movable), and (4, 5) brass leads (soldered to the Pt discs).

Dielectric measurements

Equivalent parallel capacitances and conductances were measured, between 100 Hz and 500 MHz, by Yokogawa-Hewlett-Packard (Tokyo) 4191A and 4192A impedance analyzers, each equipped with a Hewlett-Packard (HP) 16092A spring-clip fixture; both analyzers were controlled by a HP 216 computer. Measurements were made at room temperature (25 ± 1°C) immediately after extraction of lenses. Data acquisition from a single run covering 135 frequency points was completed within 3 min. Raw data thus obtained were transferred, via a GP-IB line, to another computer (PC-9801; Nippon Electric Co. Lt., Tokyo), and were routinely corrected for the effects of series inductance and stray capacitance of the measuring cell (Asami et al., 1984). Overall errors in measurement including those of electrode-distance determinations were within 10 and 15% for the lenses and nuclei, respectively.

Electron microscopy

After 1 h prefixation with 4% glutaraldehyde in 0.1 M Sörensen's phosphate buffer (pH 7.4), the lens cortex and nucleus were postfixed for 8 h with 1% osmium tetroxide in the same buffer. Fixed samples were then dehydrated in alcohol series and embedded in Spurr's resin (Spurr, 1969). Ultrathin sections were observed in a Hitachi H-300 transmission electron microscope.

EXPERIMENTAL RESULTS

When measured in the range $10^2 - 5 \cdot 10^8$ Hz, the whole lens gave rise to a complicated dielectric dispersion, or frequency dependence of its relative permittivity (ϵ) and

conductivity (κ), which was stable for at least 2 h after mounting of the specimen in spite of the molding stress exerted upon it. Fig. 2 *a* shows an averaged version of such dispersion curves collected from 10 separate experiments. It appears that, in the frequency range examined, at least two major dispersions were involved: one in the kilohertz region and the other in the lower-megahertz region. We designate these as *dispersions* 1 and 2 in the order referred to. Curve fitting was made on the basis of a two-term Cole–Cole equation as modified to include electrode polarization capacitances obeying the *m*th power law (Schwan, 1963; Asami and Irimajiri, 1984):

$$\epsilon^* - \frac{\kappa_l}{j(2\pi f)\epsilon_v} = Af^{-m} + \frac{\Delta\epsilon_1}{1 + (jf/f_{c1})^{\beta_1}} + \frac{\Delta\epsilon_2}{1 + (jf/f_{c2})^{\beta_2}} + \epsilon_h, \quad (1)$$

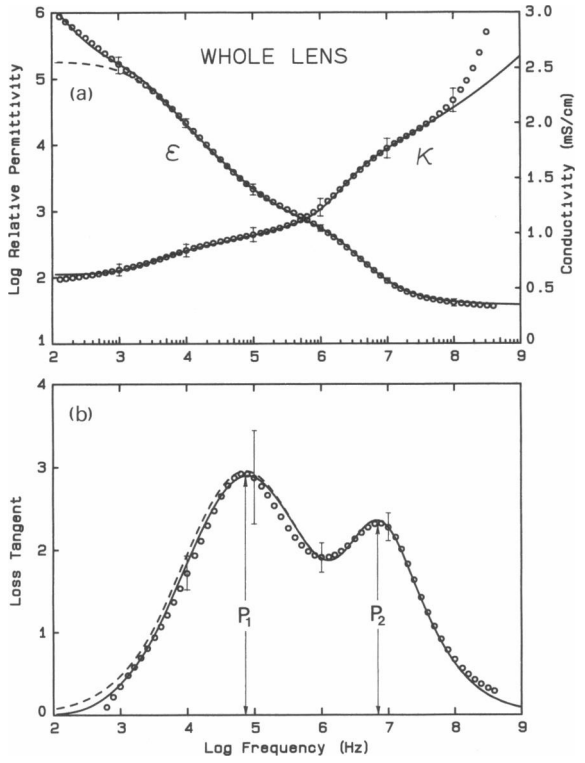

FIGURE 2 (*a*) Frequency dependence of relative permittivity (ε) and conductivity (κ) for isolated frog lenses. Each point represents a mean of data from 10 lenses. Vertical bars, ±SD. (*Solid lines*) Best fit to Eq. 1. (*Broken lines*) Corrected for the "electrode polarization" effect which is assumed to obey the *m*th power law as in Eq. 1. (*b*) Loss-tangent plot of data in *a*. P_1 and P_2 denote loss-tangent values corresponding to the low- and high-frequency peaks.

where ε* is complex relative permittivity, *f* is frequency, *A* and *m* are constants, Δε's permittivity increments, f_c's characteristic frequencies, β's the Cole–Cole parameters, numerical subscripts refer to *dispersions* 1 and 2, subscripts l and h to the limiting low- and high-frequency values, ϵ_v = 8.854 pF/m, and $j^2 = -1$. The parameter values thus obtained are listed in Table 1.

The involvement of these two dispersions is more clearly seen in Fig. 2 *b*, in which the loss tangent, $\Delta\epsilon''/\epsilon'$, is plotted against frequency. This function, a measure of energy loss in dielectrics subjected to a.c. field, has been shown to be useful in identifying dominant relaxations in biological samples also (Surowiec and Stuchly, 1986). As shown in Fig. 2 *b*, *dispersions* 1 and 2 gave rise to two corresponding peaks, which we name P_1 and P_2 inclusive of their magnitude. With frog lenses, the ratio P_1/P_2 was usually between 1.0 and 1.5. Apparently, *dispersions* 1 and 2 may be classified as the α- and β-dispersions, respectively, according to nomenclature by Schwan (Foster and Schwan, 1989). The nature and origin of *dispersion* 1 will be dealt with in the following section.

The occurrence of these multiple relaxations in the whole lens is highly likely due to the fact that this tissue comprises at least two regions each having different structural as well as physicochemical properties, namely, the nucleus and the cortex. We therefore measured denuded nuclei and cortical homogenate separately. As compared with the whole lenses, the nuclei showed a dispersion which was featured both by a lower κ-level (<0.25 mS/cm at frequencies up to 1 MHz) and by a smaller ε dispersion occurring at sub-megahertz frequencies (Fig. 3). The steep rise in ε at frequencies from 10^4 down to 10^2 Hz was of the electrode-polarization type, judging from the *m*-value involved being nearly 1.5 (Schwan, 1963). Best-fit parameter values for the nuclear dispersion are also summarized in Table 1.

Fig. 4 shows typical dispersion curves for the homogenate. Note that the cortical homogenate was several-fold more conductive than the nucleus. Digitonin treatment resulted in a suppressed permittivity increment concomitantly with a moderate elevation of κ. This fact indicates the key role played by the plasma membrane in building up the β-dispersion in the lens tissue, as previously pointed out by Pauly and Schwan (1964). However, the huge increment in ε (~10^5) and the characteristic "two-step" dispersion profile, both observed for the whole lens (Fig. 2), are most unlikely to be accounted for by simply adding the electrical properties of its component materials, without taking into consideration structural details such as fiber orientation in the lens.

Electron microscopy revealed that, in the cortical region, fiber cells with a ~2 μm width formed a highly regular array (Fig. 5 *a*), whereas in the nucleus such

TABLE 1 **Fitted values for the parameters of Eq. 1**

	ϵ_h	κ_l	$\Delta\epsilon_1$	f_{c1}	β_1	$\Delta\epsilon_2$	f_{c2}	β_2	A	m
		mS/cm		*kHz*			*MHz*		*MHz^m*	
Whole lens	38	0.63	$2 \cdot 10^5$	2	0.86	400	2	0.97	0.4	1.5
Nucleus	42	0.215	270	150	0.87	50	3	0.7	0.02	1.45

regularity in fiber orientation disappeared and the "ball-and-socket" junctions developed in a complicated fashion (Fig. 5 *b*). These features are very similar to those reported for mammalian lenses (Worgul, 1987).

ANALYSIS OF DATA

Ellipsoidal shell model

LIST OF SYMBOLS

a, b, c	semiaxes of ellipsoid
d_a, d_b	shell thicknesses corresponding to semiaxes a and b
d	mean shell thickness
ϵ^*	complex relative permittivity ($=\epsilon - j\kappa/2\pi f\epsilon_v$)
$\epsilon_a^*, \epsilon_m^*, \epsilon_i^*$	complex relative permittivities of outer (a), shell (m), and interior (i) phases of ellipsoid
$\bar{\epsilon}_k^*$	effective permittivity of shelled ellipsoid along $k(=x, y, z)$-axis
A_{ik}, A_k	depolarization factors for inner and outer spheroids
ϵ_k^*	suspension permittivity for ellipsoids oriented along $k(=x, y, z)$-axis
ϵ_r^*	suspension permittivity for ellipsoids in random orientation
Φ	volume fraction

We assume a prolate spheroid (Fig. 6) as a model for the lens fiber cells, although their real shape was hexagonal in cross-section. Suppose an ellipsoid of revolution with semiaxes a, b, and c ($=b$), the inside of which is occupied by another confocal ellipsoid of complex permittivity ϵ_i^* so as to leave an average clearance d between the two spheroidal surfaces (Fig. 6 *a*); the space between is meant for the membrane and thus assigned ϵ_m^*. In this model, the membrane thickness is assumed not to exceed 1% of the length of either semiaxis. Under this condition, i.e.,

$$d_a \ll a \text{ and } d_b \ll b, \tag{2}$$

the mean shell thickness d is given (Appendix 1) by

$$d \approx 0.85\, d_b \tag{3}$$

for axial ratios (b/a) of 1:5 or less.

Effective complex relative permittivity ($\bar{\epsilon}_k^*$) that represents the shell-covered ellipsoid as seen from one of the directions along its principal axes has been derived by Saito et al. (1966) and Asami et al. (1980*a*,*b*), and this may be written as

$$\bar{\epsilon}_k^* = \epsilon_m^* \frac{\epsilon_m^* - (\epsilon_i^* - \epsilon_m^*)A_{ik} + v(\epsilon_i^* - \epsilon_m^*)(1 - A_k)}{\epsilon_m^* - (\epsilon_i^* - \epsilon_m^*)A_{ik} - v(\epsilon_i^* - \epsilon_m^*)A_k}, \quad (k = x, y, z). \tag{4}$$

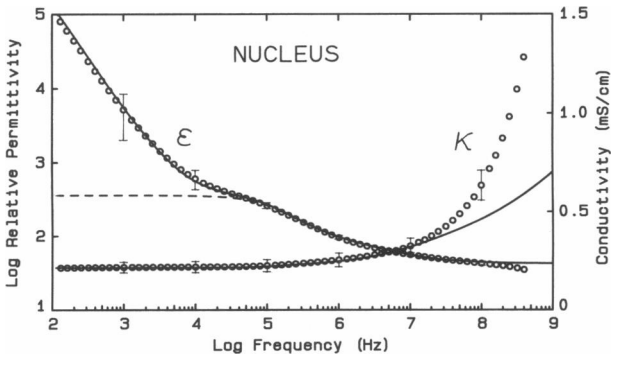

FIGURE 3 Frequency dependence of relative permittivity (ϵ) and conductivity (κ) for isolated nuclei. Each point represents a mean data from three nuclei. Vertical bars, ±SEM. (*Solid lines*) Best fit to Eq. 1. (*Broken lines*) Corrected for the "electrode polarization" effect which is assumed to obey the mth power law as in Eq. 1.

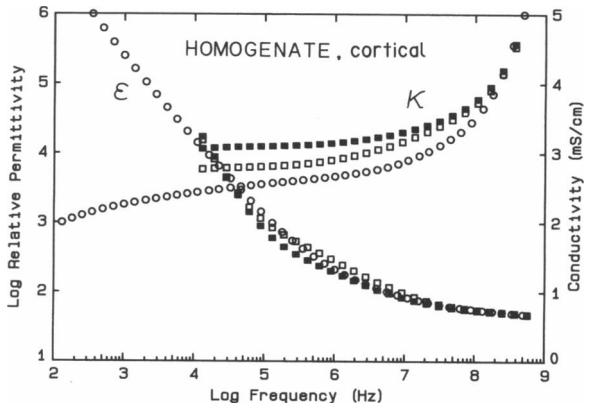

FIGURE 4 Plots of relative permittivity (ϵ) and conductivity (κ), as a function of frequency, for cortical homogenate (○, □) from 2 separate lenses and for the homogenate (marked "□") treated with 2% (wt/vol) digitonin (■).

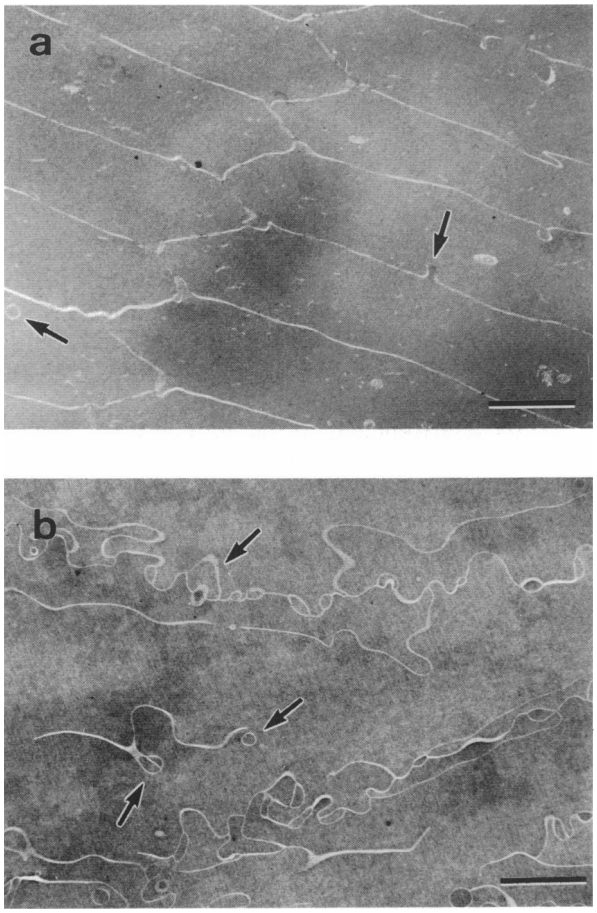

FIGURE 5 Transmission electron micrographs of a frog lens. (*a*) Cortical fiber cells in transverse section; (*b*) nuclear region. Arrows indicate characteristic "ball-and-socket" junctions between adjacent cells. Bars, 2 μm.

Here, A_{ik} and A_k, which both depend solely on the axial ratios, are the depolarization factors for the inner and outer spheroids, respectively, and v is the fractional volume of the inner spheroid, defined by

$$v = (1 - d/a)(1 - d/b)^2. \tag{5}$$

If $A_{ik} \approx A_k$, a sequel of condition 2, Eq. 4 reduces to

$$\bar{\epsilon}_k^* = \epsilon_m^* + v\left[\frac{1}{\epsilon_i^* - \epsilon_m^*} + (1 - v)\frac{A_k}{\epsilon_m^*}\right]^{-1}, (k = x, y, z) \tag{6}$$

with

$$A_x = \frac{-1}{q^2 - 1} + \frac{q}{(q^2 - 1)^{3/2}} \ln\left[q + (q^2 - 1)^{1/2}\right], (q = a/b) \tag{7}$$

$$A_y = A_z = (1 - A_x)/2. \tag{8}$$

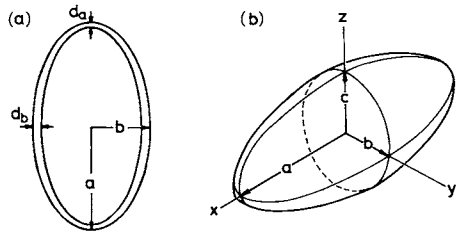

FIGURE 6 Ellipsoidal shell model.

Next, we will write down expressions for these ellipsoids in suspension. Sillars (1937) extended Maxwell–Wagner's mixture theory to include the suspensions of oriented nonspherical particles (for a recent review, see e.g., Takashima, 1989). Sillars' equation for a very dilute suspension (complex permittivity as seen from direction k, ϵ_k^*) of prolate spheroids ($\bar{\epsilon}_k^*$) dispersed *orientedly* in a medium of ϵ_a^* can be expressed in the form

$$\epsilon_k^* = \epsilon_a^* + \Phi\frac{\epsilon_a^*(\bar{\epsilon}_k^* - \epsilon_a^*)}{\epsilon_a^* + (\epsilon_k^* - \epsilon_a^*)A_k}, (k = x, y, z), \tag{9}$$

where Φ is volume fraction and A_k is the depolarization factor, as before. Owing to the assumption that $\epsilon_k^* \approx \epsilon_a^*$ used in its derivation, Eq. 9 is valid only for $\Phi \ll 1$. To deal with concentrated systems like the lens tissue ($\Phi > 0.8$), therefore, we have to extend Eq. 9 to a form applicable to higher Φ's. Several authors have already derived closed-form equations along this line (Boned and Peyrelasse, 1983; Boyle, 1985). However, we shall make another approach below because those existing theories fail to cover randomly oriented suspensions.

Applying Hanai's incremental method (Hanai, 1960), namely, the replacement of members in Eq. 9 such that

$$\epsilon_a^* \to \epsilon_k^*, \epsilon_k^* \to \epsilon_k^* + \Delta\epsilon_k^*, \text{ and } \Phi \to \Delta\Phi'/(1 - \Phi'),$$

we have a differential form:

$$\Delta\epsilon_k^* = \frac{\Delta\Phi'}{1 - \Phi'}\left[\frac{1}{\bar{\epsilon}_k^* - \epsilon_k^*} + \frac{A_k}{\epsilon_k^*}\right]^{-1}, (k = x, y, z). \tag{10}$$

This relation, if combined with Eq. 6, provides us with an increment $\Delta\epsilon_k^*$ due to a small increment $\Delta\Phi'$ ($=\Phi/100$, for instance) in the volume fraction of the suspended phase. Numerical integration of Eq. 10 with respect to ϵ_k^* and Φ' over the ranges $[\epsilon_a^*, \epsilon_k^*]$ and $[0, \Phi]$, respectively, yields the final suspension permittivities, ϵ_x^*, ϵ_y^*, and ϵ_z^*.

For concentrated *random* suspensions with permittivity ϵ_r^*, its small increment $\Delta\epsilon_r^*$ may be expressed as an average taken over the three $\Delta\epsilon_k^*$'s, each being given by Eq. 10, in which ϵ_k^*'s on the right-hand side are replaced

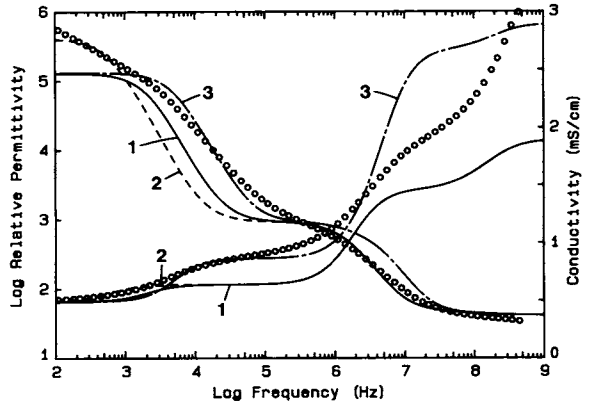

FIGURE 7 Illustration of curve fitting based on the random orientation model. Data are from a typical case of the whole lens, not corrected for the electrode polarization. Curves 1–3 correspond to the parameter values in Table 2.

by ϵ_r^*. Now we have

$$\Delta\epsilon_r^* = \frac{1}{3}\cdot\frac{\Delta\Phi'}{1-\Phi'}\sum_{k=x,y,z}\left[\frac{1}{\epsilon_k^*-\epsilon_r^*}+\frac{A_k}{\epsilon_r^*}\right]^{-1}. \qquad (11)$$

Based on Eqs. 6 and 11, the suspension permittivity ϵ_r^* can likewise be obtained by numerical integration.

Evaluation of random and oriented models

Fig. 7 illustrates comparison between theory and experiment. Theoretical curves refer to calculations for the random model (Eq. 11) employing the parameter values listed in Table 2. Experiment refers to a typical set of dielectric data on a whole lens. In this calculation, we have assumed that the ϵ and κ of the extracellular fluid are the same as those of frog Ringer's and that the membrane is several orders of magnitude less conducting than the surrounding phase, a reasonable assumption for the membrane of fiber cells. A value of 2 μm, estimated from electron microscopy (Fig. 5), is used for the fiber width (i.e., the minor semiaxis in the model is fixed at 1 μm), while leaving the fiber length (or the major semiaxis) adjustable. Parameter values for the cell interior (ϵ_i and κ_i) are taken from measurements on the homogenate. The *random* ellipsoidal shell model generates undulating dispersion curves, which could mimic, to a certain extent, the general features of the observed. However, even in the best fit (Fig. 7, *curves 3*), fitting is far from being satisfactory especially at frequencies above 10^5 Hz.

Theoretical dispersion curves calculated from the *oriented* shell model are shown in Fig. 8. In this case, we have two choices with respect to the direction of fiber alignment: the cells' axes of symmetry are aligned either parallel or perpendicular to the applied field. With the same set of parameter values employed (*a:b:c* [in micrometers] = 100:1:1, Φ = 0.85, etc.), the parallel model leads to a huge dispersion around 10^4 Hz (*curves* E), whereas the perpendicular model to a smaller dispersion around 10^7 Hz (*curves* P). Thus it is clear that either choice alone cannot simulate the observed dielec-

TABLE 2 Fitted values for the parameters of the random orientation model (Eqs. 6 and 11) as applied to data in Fig. 7

Curve	Semiaxes (*a/b/c*)	ϵ_i	κ_i	Φ
	μm		mS/cm	
1	100/1/1	40	0.8	0.85
2	200/1/1	40	0.8	0.85
3	100/1/1	40	2.0	0.85

Assumed parameter values are: ϵ_a = 75, κ_a = 12 mS/cm, ϵ_m = 5, κ_m = 0.1 nS/cm, and d = 8 nm.

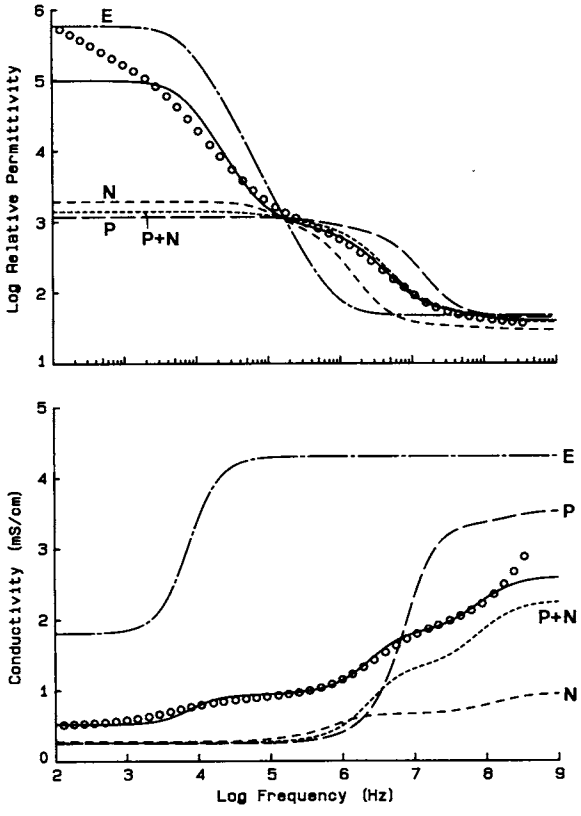

FIGURE 8 Illustration showing the procedure for curve fitting based on the allocation model (Eq. 15). Experimental data, same as in Fig. 7. Solid curves refer to the best fit obtained using the parameters in Table 3. Curves E, P, and N depict the theoretical, elemental dielectric behavior of the E-, P-, and N-regions. Curve "P + N" refers to a series synthesis of P and N.

tric behavior as long as these "regular" orientation models are naively employed throughout. This awareness prompts us to introduce a macro-model that matches in any way regional differences in the actual fiber orientation.

Equivalent circuit for the whole lens

This is illustrated in Fig. 9. When neglecting a possible but small contribution of the capsule and epithelium to the bulk properties, the discoid-molded lens can be regarded as consisting of the following three main regions: equatorial cortex (E), polar cortex (P), and nucleus (N). For each of these, its permittivity and fractional volume are respectively denoted by ϵ^* and V, both suffixed E, P, or N. In an equivalent circuit (Fig. 9 *b*), admittance Y for the whole lens may be expressed as a parallel combination of admittances for the equatorial and central regions (Y_E and Y_C), whereas Y_C is a lumped admittance for a series combination of Y_P and Y_N, so that

$$Y = Y_E + Y_C \tag{12}$$

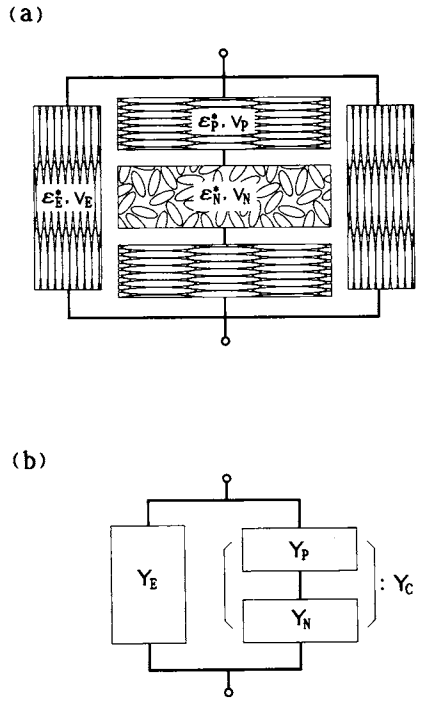

FIGURE 9 (*a*) Schematic illustration of fiber orientation in the three major parts (E, P, and N) that comprise the whole lens. ϵ^*'s and V's refer respectively to complex relative permittivities and fractional volumes for the three elements. (*b*) Equivalent circuit for the whole lens as represented by a combination of three admittances (Y's) corresponding to the E, P, and N.

and

$$1/Y_C = 1/Y_P + 1/Y_N. \tag{13}$$

On the other hand, admittances, Y_E, Y_P, and Y_N, are related to the corresponding parameters, ϵ^*'s and V's, that represent the E, P, and N (Appendix 2). Substituting these in Eqs. 12 and 13, and noting that

$$V_E + V_P + V_N = 1, \tag{14}$$

we obtain an expression for the whole lens permittivity:

$$\epsilon^* = V_E \epsilon^*_E + (1 - V_E)^2(V_P/\epsilon^*_P + V_N/\epsilon^*_N)^{-1} \tag{15}$$

Because ϵ^*_E, ϵ^*_P, and ϵ^*_N are represented by ϵ^*_x, ϵ^*_y, and ϵ^*_r, respectively, the overall permittivity ϵ^* can then be calculated from Eq. 15 combined with Eqs. 6, 10, and 11, given the values of V_E, V_P and V_N. We name this model (Eq. 15) an allocation model.

Simulation with an allocated ellipsoidal-shells model

We begin by estimating the V_E, V_P, and V_N. As the degrees of cell packing in different regions may differ we denote the respective cell volume fractions by Φ_E, Φ_P, and Φ_N. Literature values for the extracellular space of decapsulated toad lenses range from 1.2% to 34%, depending on the methods and space markers used (Paterson, 1970; Yorio and Bentley, 1976), so we assume that $\Phi_N = 0.9$ and further that $\Phi_N > \Phi_E = \Phi_P$ because the nucleus is more compactly packed than the cortex and both the Φ_E and Φ_P pertain to the same cortical region. The dimensions of cells, *a*:*b*:*c* (in micrometers), are again assigned 100:1:1 and 5:1:1 for the cortex and nucleus, respectively. Other assumed parameters are listed in Table 3. Under these conditions, we can determine, via curve fitting, the volume ratios as V_E: V_P:V_N = 3 ± 0.3 : 9.5 ± 0.6 : 5.7 ± 0.6 (mean ± SEM, n = 5) with $\Phi_E = \Phi_P = 0.85$. The procedure will be detailed in Appendix 3.

The results of simulation based on the allocation

TABLE 3 **Fitted values for the parameters of the allocated ellipsoidal-shells model (Eqs. 6, 10, 11, and 15) as applied to data in Fig. 7**

Lens region	Fiber orientation	Semiaxes (*a*/*b*/*c*)	V	ϵ_i	κ_i	Φ
		μm			*mS/cm*	
E	Parallel	100/1/1	0.167	45	3.0	0.85
P	Perpendicular	1/1/100	0.555	45	3.0	0.85
N	Random	5/1/1	0.278	28	0.3	0.9

Assumed parameter values are: ϵ_a = 75, κ_a = 12 mS/cm, ϵ_m = 5, κ_m = 0.1 nS/cm, and d = 8 nm.

model are summarized in Table 3, with the best-fit curves depicted in Fig. 8 (*solid lines*).

Simulation with the allocation model that allows fiber size distribution

As seen from Fig. 8, the quality of curve fitting for *dispersion* 1 was rather poor compared with *dispersion* 2, leaving sizeable discrepancy between theory and experiment. One reason for this may be the oversimplification, among others, in our modeling that the cortical fibers were allotted a uniform length of 0.2 mm throughout. In the actual tissue, however, the effective "straight" fiber lengths must be distributed over a certain range. Therefore, we attempt to divide the E-region into several *sub*regions of different fiber sizes. The results of calculations with this distribution model as applied to five possible cases are shown in Table 4, from which one may evaluate the goodness of fitting in terms of the minimized residual. It is clear from Table 4 that, among these distributions, the case of 0.5/0.4/0.2/0.1 mm with a corresponding "volume fraction" assignment of [15%/28%/29%/28%] can be the most plausible explanation. This particular case is illustrated in Fig. 10, which clearly shows substantial improvement in fitting for *dispersion* 1.

DISCUSSION

We have shown that the dielectric behavior of isolated lenses can be simulated by introducing a realistic model that may represent both the characteristic shape of fiber cells and, in addition, their anisotropic orientation inside the tissue. Of particular interest are the conditions required for detecting *dispersion* 1 separate from *dispersion* 2, the mechanisms of these two *sub*dispersions, the regional difference in the deduced parameter values, and the applicability of the present method to the analysis of cataractous lenses. These points are discussed in turn.

Detection of *dispersion* 1 has been made possible through the maneuver of molding lenses into discoid so as to fill the cell cavity with specimen as fully as possible. In a preliminary test, we mounted intact lenses without this maneuver while filling the gap between electrode and specimen with Ringer's solution. This setting, however, led to a featureless (nonundulant) dispersion curve of the electrode polarization type at frequencies up to 10^5 Hz, and so we failed to locate *dispersion* 1. Similar nonundulant dispersions of lowered magnitude were also observed at the same audio frequencies when the

TABLE 4 Summary of percent residuals, $R(\epsilon)$ and $R(\kappa)$, as a measure of the goodness of curve fitting when size distribution is introduced in the E region

Fiber length/*mm* (Volume fraction/%)	10^2–$5 \cdot 10^8$ Hz			10^3–10^5 Hz		
	$R(\epsilon)$	$R(\kappa)$	Mean	$R(\epsilon)$	$R(\kappa)$	Mean
0.2 (100)	3.2	1.8	2.5	6.2	16.7	14.1
0.4/0.2 (50/50)	1.9	1.6	1.7	5.0	13.1	9.0
0.4/0.2/0.1 (33/34/33)	2.0	1.4	1.7	3.1	8.1	5.6
0.5/0.4/0.2/0.1 (15/28/29/28)	1.3	1.1	1.2	1.4	2.8	2.1
0.5/0.4/0.2/0.1 (25/25/25/25)	1.2	1.3	1.3	1.5	5.9	3.7
1.0/0.5/0.4/0.2/0.1 (11/22/22/23/22)	1.4	2.0	1.7	4.5	20.3	12.4

Residuals are defined, separately for ϵ and κ, as

$$R(\epsilon) = \frac{\sum |\log \epsilon_{obs} - \log \epsilon_{theor}|}{\Delta \log \epsilon_{obs}} \times \frac{100}{n}$$

$$R(\kappa) = \frac{\sum |\kappa_{obs} - \kappa_{theor}|}{\Delta \kappa_{obs}} \times \frac{100}{n},$$

where Δ denotes difference between the maximum and the minimum of relevant observed values within the frequency range considered. n is the number of frequency points covered by that range. The observation refers to data in Fig. 10. Theoretical values are from the allocated ellipsoidal-shells model (Eqs. 6, 10, 11, and 15) as extended to distributed cell lengths in the E region.

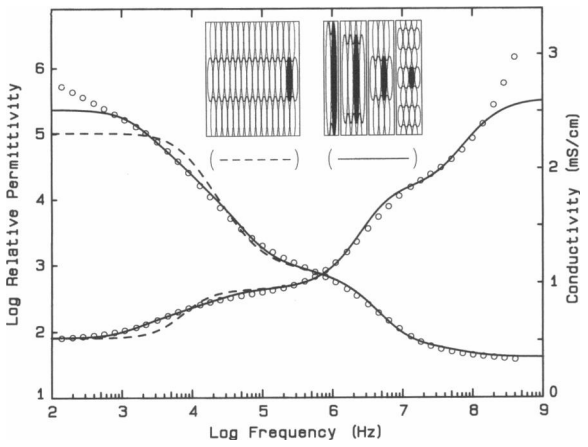

FIGURE 10 Effect of fiber-length distribution in the equatorial cortex (*inset*) upon the fitted dielectric behavior. Data, same as in Fig. 8. (*Inset: left*) No distribution ($2a$ = 200 μm); (*right*) distribution such that $2a$ = 500 μm (15%), 400 μm (28%), 200 μm (29%), and 100 μm (28%). (*Solid line*) Best fit with these distributed fiber lengths for the E-region. (*Broken line*) Same as the best-fit shown in Fig. 8. Other parameter values are the same as in Table 3.

specimens were only partly damaged either by pricks through the capsule to the depth of ~1.5 mm over the entire anterior hemisphere, or by subjecting the specimens to "mount/demount" manipulations repeated several times. Hence it seems likely that the normal ordered arrangement of cortical fibers *in situ* is essential for a successful detection of *dispersion* 1. This in turn implies that some subtle mechanisms involved in the lens cortex would account for *dispersion* 1.

Of the two major dispersions described here, *dispersion* 2 with a center relaxation frequency f_c of 2 MHz is highly likely due to the Maxwell-Wagner effect, or interfacial polarization at the surface of cell membrane (Pauly and Schwan, 1964). In contrast, *dispersion* 1 with a $\Delta\epsilon$ of 10^5 and an f_c of 2–4 kHz has not so far been reported for the lens tissue. Apparently, this is of the type termed α-dispersion, whose center frequencies are claimed to fall in the range 0.1–10 kHz (Schwan, 1957).

Several mechanisms have been proposed for the origin of the α-dispersion. These include polarization of counterions near the membrane surface, charging of intracellular membrane systems, and again the Maxwell-Wagner effect in elongated cells placed parallel to the applied field (Schwan, 1957; Foster and Schwan, 1989). In muscle, the α-dispersion has been related to the sarcotubular system (Foster and Schwan, 1989), whereas the lens cells lack such tubular systems or the like. According to Falk and Fatt (1964), the counterion polarization mechanism premises an unusually high fixed-charge density, the extent of which is presently unknown for the lens cell membrane. Even so, a mere mechanical perturbation of fiber arrays or cell injury, mentioned above, is unlikely to affect the state of surface charges.

Thus, it appears that the Maxwell-Wagner effect is the most plausible, if not the sole, explanation for *dispersion* 1. In fact, the cortical fibers are long and thin and run mostly parallel to the field in the equatorial region (Worgul, 1987). Some of them are extending well over 1 mm. Such a length of pertinent cells may well cause a large dispersion in the kilohertz region, as a result of interfacial polarization. In this regard, it may be relevant to note that a range of cortical fiber sizes (0.1–0.5 mm) with a mean of ~0.2 mm are "effective straight" lengths that have been estimated through curve fitting. Indeed, it is possible, especially in the equatorial cortex, that these "effective" sizes are distributed because the radii of curvature for concentric layers should decrease with increasing depth. Hence, this effect has been postulated as a likely mechanism for the observed broadening of *dispersion* 1. Despite the gross success of the analysis presented above, it should however be noted that the counterion polarization still remains to be a mechanism which is responsible for the observed low-frequency behavior of the lens. A method for estimating this latter effect is simply lacking at present.

With the simplest possible modeling in view, we have dichotomized the whole lens into "cortex" and "nucleus," neglecting the intermediate transition zone. Based on this model, which might be called an "electrical dissection" model, a fractional volume of ~30% has been determined for the nucleus. Also, the degree of cell packing in the cortex turned out to be 85%, if the nuclear counterpart was set at 90%. These are the first *noninvasive* estimates made for intact lenses. The deduced ϵ and κ values for the cell interior (Table 3) are in a reasonable range in light of the fact that the lens is a relatively dehydrated tissue of high protein concentration. The finding that the nuclear levels of ϵ_i and κ_i are reduced compared with the cortical ones is considered to reflect the reported regional differences such that water content is smaller in the nucleus than in the cortex (Rink, 1978).

The dielectric spectroscopy, when complemented by a proper analysis, can provide otherwise inaccessible information. For instance, a preliminary test in our laboratory indicated that the present method is useful for detecting early cataractous changes that are so faint as to escape the conventional turbidometric examination. Specifically, *dispersion* 1 was found to be sensitive to changes in the cortical membrane conductivity that were induced by cataractogenic agents. These changes can be quantitativey followed in terms of the loss tangent ratio P_1/P_2 (Watanabe M., T. Suzaki, and A. Irimajiri, unpub-

lished observation). This study purports, on one hand, to provide a physical basis for the proper interpretation of these findings, and on the other hand, to develop a nondestructive method whereby to probe into complex biological tissues including the crystalline lens. As such, the impedance approach described here is promising.

APPENDIX 1

Effective thickness of ellipsoidal shell

The volume of the space between the two confocal ellipsoids (Fig. 6 *a*) is given by

$$V_1 = (4\pi/3)[ab^2 - (a - d_a)(b - d_b)^2],$$

which under the condition of text inequalities 2 along with the confocality requirement, i.e., $ad_a \simeq bd_b$, reduces to

$$V_1 + (4\pi/3)\, ab\,(2 + p^2)\, d_b$$

with $p = b/a$.

On the other hand, the volume of an ellipsoidal shell with a uniform thickness d ($d_a < d < d_b$) may be approximated by

$$V_2 = 2\pi ab[p + (1 + p^2/2)\,\mathrm{Cos}^{-1}p]d.$$

Equating V_1 to V_2, we have

$$d/d_b = (2/3)(2 + p^2)/[p + (1 + p^2/2)\,\mathrm{Cos}^{-1}p].$$

Thus the d/d_b ratio is calculated to be 0.851 for $p = 1/5$ and to be 0.849 for $p = 1/50$ or less, leading to text Relation 3.

APPENDIX 2

Expressions for Y, Y_E, Y_P, and Y_N, and derivation of Eq. 15

Admittance Y for a block of material of ϵ^* may be written

$$Y = j\omega\epsilon_v\epsilon^*(S/t), \tag{A1}$$

where S is cross-section and t is thickness. Similarly, the three admittances appearing in our lens model (Fig. 9 *b*) are given by

$$Y_x = j\,\omega\epsilon_v\epsilon_x^*(S_x/t_x) \quad \text{with } x = \mathrm{E, P, and N}. \tag{A2}$$

In our modeling depicted in Fig. 9, the following simplified geometry has been assumed:

$$S = S_E + S_C$$
$$S_C = S_P = S_N$$
$$t = t_E = t_P + t_N.$$

Putting $S/t = r$, $S_N/t_N = r_N$ and so forth, and recalling the normalizing condition (text Eq. 14), one obtains from the above geometrical requirements

$$r = r_N V_N/(1 - V_E)^2$$
$$r_E = r_N V_N V_E/(1 - V_E)^2$$
$$r_P = r_N V_N/V_P.$$

Substituting these ratios in Eqs. A1 and A2, and further substituting those resultant expressions for Y and Y_x's in Eqs. 12 and 13 lead to text Eq. 15.

APPENDIX 3

Determination of V_E, V_P, V_N and Φ_P

Curve fitting is made preferentially on the conductivity dispersion (Fig. 8 *b*).

As the two components "E" and "P + N", in our model (Fig. 9) have been assumed to be in a parallel arrangement, the resultant conductivity κ is given by a weighted mean of conductivities for both components:

$$\kappa = V_E\kappa_E + (V_P + V_N)\,K_{P+N}. \tag{A3}$$

Consequently, at the low frequency limit,

$$\kappa_l = V_E\kappa_{l,E} + (V_P + V_N)\kappa_{l,P+N}. \tag{A4}$$

For increments, $\Delta\kappa$'s, due to dispersion in the same frequency range,

$$\Delta\kappa = V_E\Delta\kappa_E + (V_P + V_N)\Delta\kappa_{P+N}. \tag{A5}$$

Values of $\Delta\kappa_E$ predictable from the parallel orientation model (text Eq. 10) are: $\Delta\kappa_E$ = 2.35, 2.50, and 2.64 mS/cm for Φ_E = 0.8, 0.85, and 0.9, respectively. The observed conductivity increment for *dispersion* 1 ($\Delta\kappa_l$) is 0.42 mS/cm. Over the corresponding frequency range (10^2–10^5 Hz), the calculated values of $\Delta\kappa_P$ and $\Delta\kappa_N$ are almost nil for any Φ's between 0.8 and 0.9, and hence $\Delta\kappa_{P+N} \simeq 0$. Substituting these $\Delta\kappa$-values in Eq. A5, we obtain

$$V_E \simeq 1/6 \tag{A6}$$

and

$$V_P + V_N \simeq 5/6. \tag{A7}$$

Substituting Eqs. A6 and A7 in Eq. A4, and rearranging,

$$\kappa_{l,P+N} = (6\kappa_l - \kappa_{l,E})/5. \tag{A8}$$

As seen from Fig. 8 *b*, curve *E* (for Φ_E = 0.85) levels off at 10^5 Hz or higher. Calculations show that the same is true for $0.8 < \Phi_E < 0.9$. This implies that at frequencies higher than 10^5 Hz, where *dispersion* 2 takes place, $\Delta\kappa_E \simeq 0$, so that Eq. A5, as applied to *dispersion* 2, reduces to

$$\Delta\kappa_2 = (V_P + V_N)\,\Delta\kappa_{P+N} = (5/6)\,\Delta\kappa_{P+N}. \tag{A9}$$

On the other hand, given the values of Φ_E, we can calculate $\kappa_{l,E}$'s, and thereupon the corresponding $\kappa_{l,P+N}$'s, using Eq. A8 as

$$\kappa_{l,P+N} = \begin{Bmatrix}0.142\\0.262\\0.382\end{Bmatrix} \text{mS/cm for } \Phi_E = \begin{Bmatrix}0.8\\0.85.\\0.9\end{Bmatrix} \tag{A10}$$

Likewise, $K_{l,P}$ is calculated, according to text Eq. 10 as

$$\kappa_{l,P} = \begin{Bmatrix}0.465\\0.257\\0.110\end{Bmatrix} \text{mS/cm for } \Phi_P = \begin{Bmatrix}0.8\\0.85.\\0.9\end{Bmatrix} \tag{A11}$$

The low-frequency limit level $\kappa_{l,N}$ is calculated from text Eq. 11 to be 0.280 mS/cm for Φ_N = 0.9. The series arrangement of P and N requires that $\kappa_{l,P+N}$ be in between $\kappa_{l,P}$ and $\kappa_{l,N}$, irrespective of the ratio V_P/V_N. Upon inspection of Eqs. A10 and A11 under the restraint, $\Phi_E = \Phi_P$, therefore, we find that the only feasible case is $K_{l,P+N}$ = 0.262 mS/cm.

Hence

$$\Phi_E = \Phi_P = 0.85. \quad \text{(A12)}$$

Curves P and N (Fig. 8) refer to calculations employing the stated size parameters with $\Phi_P = 0.85$ and $\Phi_N = 0.9$.

For the determination of V_P/V_N, we take note of Eq. A9. Substituting the observed value of $\Delta\kappa_2$ (= 1.15 mS/cm) in Eq. A9, we have

$$\Delta\kappa_{P+N} \simeq 1.4 \text{ mS/cm}. \quad \text{(A13)}$$

A computer search, based on text Eq. 13, for the condition that satisfies Eq. A13 has yielded

$$V_P/V_N = 0.556/0.278 = 2/1. \quad \text{(A14)}$$

The curves marked "P+N" (Fig. 8) refer to a series synthesis which is made by using the above values of V_P and V_N. Thus we have reached a regional volume assignment:

$$V_E : V_P : V_N : = 3 : 10 : 5. \quad \text{(A15)}$$

We thank Dr. K. Asami and Dr. T. Hanai, Kyoto University, for stimulating discussions of the ellipsoidal model. Thanks are also due to Dr. A. Tamai and Dr. H. Ueno for helpful suggestions.

This study was supported in part by grants (no. 62870101 and 01772025) from The Ministry of Education, Science and Culture, Japan.

Received for publication 25 June 1990 and in final form 14 August 1990.

REFERENCES

Asami, K., T. Hanai, and N. Koizumi. 1980*a*. Dielectric approach to suspensions of ellipsoidal particles covered with a shell in particular reference to biological cells. *Jpn. J. Appl. Phys.* 19:359–365.

Asami, K., T. Hanai, and N. Koizumi. 1980*b*. Dielectric analysis of *Escherichia coli* suspensions in the light of the theory of interfacial polarization. *Biophys. J.* 31:215–228.

Asami, K., and A. Irimajiri. 1984. Dielectric analysis of mitochondria isolated from rat liver. II. Intact mitochondria as simulated by a double-shell model. *Biochim. Biophys. Acta.* 778:570–578.

Asami, K., A. Irimajiri, T. Hanai, N. Shiraishi, and K. Utsumi. 1984. Dielectric analysis of mitochondria isolated from rat liver. I. Swollen mitoplasts as simulated by a single-shell model. *Biochim. Biophys. Acta.* 778:559–569.

Boned, C., and J. Peyrelasse. 1983. Etude de la permittivite complexe d'ellipsoides disperses dans un milieu continu. Analyses theorique et numerique. *Colloid & Polym. Sci.* 261:600–612.

Boyle, M. H. 1985. The electrical properties of heterogeneous mixtures containing an oriented spheroidal dispersed phase. *Colloid & Polym. Sci.* 263:51–57.

Dawkins, A. W. J., C. Gabriel, R. J. Sheppard, and E. H. Grant. 1981. Electrical properties of lens material at microwave frequencies. *Phys. Med. Biol.* 26:1–9.

Duncan, G. 1969*a*. Relative permeabilities of the lens membranes to sodium and potassium. *Exp. Eye Res.* 8:315–325.

Duncan, G. 1969*b*. The site of the ion restricting membranes in the toad lens. *Exp. Eye. Res.* 8:406–412.

Duncan, G. 1969*c*. Kinetics of potassium movement across amphibian lens membrane. *Exp. Eye. Res.* 8:413–420.

Eisenberg, R. S., and J. L. Rae. 1976. Current-voltate relationships in the crystalline lens. *J. Physiol.* 262:285–300.

Falk G., and P. Fatt. 1964. Linear electrical properties of striated muscle fibers observed with intracellular electrodes. *Proc. R. Soc. Lond. Ser. B.* 160:69–123.

Foster, K. R., and H. P. Schwan. 1989. Dielectric properties of tissues and biological materials: a critical review. *Crit. Rev. Biomed. Eng.* 17–1:25–104.

Gabriel, C., R. J. Sheppard, and E. H. Grant. 1983. Dielectric properties of ocular tissues at 37°C. *Phys. Med. Biol.* 28:43–49.

Hanai, T. 1960. Theory of dielectric dispersion due to the interfacial polarization and its application to emulsion. *Kolloid Z.* 171:23–31.

Mathias, R. T., J. L. Rae, and R. S. Eisenberg. 1979. Electrical properties of structural components of the crystalline lens. *Biophys. J.* 25:181–201.

Mathias, R. T., J. L. Rae, and R. S. Eisenberg. 1981. The lens as a nonuniform spherical syncytium. *Biophys. J.* 34:61–83.

Paterson, C. A. 1970. Extracellular space of the crystalline lens. *Am. J. Physiol.* 218:797–802.

Pauly, H., and H. P. Schwan. 1964. The dielectric properties of the bovine eye lens. *IEEE (Inst. Electr. Electron. Eng.) Trans. Biomed. Eng.* 11:103–109.

Rae, J. L., R. T. Mathias, and R. S. Eisenberg. 1982. Physiological role of the membranes and extracellular space within the oclar lens. *Exp. Eye Res.* 35:471–489.

Rink, H. 1978. The water content in bovine lenses during aging. *Interdiscipl. Topics Geront.* 12:271–277.

Saito, M., H. P. Schwan, and G. Schwarz. 1966. Response of nonspherical biological particles to alternating electric fields. *Biophys. J.* 6:313–327.

Schwan, H. P. 1957. Electrical properties of tissue and cell suspensions. *In* Advances in Biological and Medical Physics. J. H. Lawrence and C. A. Tobias, editors. Academic Press, New York. 5:147–209.

Schwan, H. P. 1963. Determination of biological impedances. *In* Physical Techniques in Biological Research. Part B. W. L. Nastuk, editor. Academic Press, New York. 6:323–407.

Sillars, R. W. 1937. The properties of a dielectric containing semiconducting particles of various shapes. *J. Inst. Elec. Engrs.* 80:378–394.

Spurr, A. R. 1969. A low-viscosity epoxy resin embedding medium for electron microscopy. *J. Ultrastruct. Res.* 26:31–43.

Surowiec, A., and S. S. Stuchly. 1986. Use of the loss-tangent function in dielectric spectroscopy. *Bioelectromagnetics.* 7:259–269.

Takashima, S. 1989. Electrical Properties of Biopolymers and Membranes. Adam Hilger, Bristol and Philadelphia. 396 pp.

Worgul, B. V. 1987. The lens. *In* Biomedical Foundation of Ophthalmology. T. D. Duane and E. A. Jaeger, editors. Harper and Row, Philadelphia, PA. 1:1–33.

Yorio, T., and P. J. Bentley. 1976. Distribution of the extracellular space of the amphibian lens. *Exp. Eye Res.* 23:601–608.